Insufficient Gas Accretion Caused the Decline in Cosmic Star-formation Activity Eight Billion Years Ago

Aditya Chowdhury , Nissim Kanekar , and Jayaram N. Chengalur
National Centre for Radio Astrophysics, Tata Institute of Fundamental Research, Pune, India; chowdhury@ncra.tifr.res.in

Abstract

Measurements of the atomic hydrogen (HI) properties of high-redshift galaxies are critical to understanding the decline in the star formation rate (SFR) density of the universe after its peak $\approx 8–11$ Gyr ago. Here, we use ≈ 510 hr of observations with the upgraded Giant Metrewave Radio Telescope to measure the dependence of the average HI mass of star-forming galaxies at $z = 0.74–1.45$ on their average stellar mass and redshift by stacking their HI 21 cm emission signals. We divide our sample of 11,419 main-sequence galaxies at $z = 0.74–1.45$ into two stellar-mass (M_*) subsamples, with $M_* > 10^{10} M_\odot$ and $M_* < 10^{10} M_\odot$, and obtain clear detections, at $>4.6\sigma$ significance, of the stacked HI 21 cm emission in both subsamples. We find that galaxies with $M_* > 10^{10} M_\odot$, which dominate the decline in the cosmic SFR density at $z \lesssim 1$, have HI reservoirs that can sustain their SFRs for only a short period, 0.86 ± 0.20 Gyr, unless their HI is replenished via accretion. We also stack the HI 21 cm emission from galaxies in two redshift subsamples, at $z = 0.74–1.25$ and $z = 1.25–1.45$, again obtaining clear detections of the stacked HI 21 cm emission signals, at $>5.2\sigma$ significance in both subsamples. We find that the average HI mass of galaxies with $\langle M_* \rangle \approx 10^{10} M_\odot$ declines steeply over a period of ≈ 1 billion years, from $(33.6 \pm 6.4) \times 10^9 M_\odot$ at $\langle z \rangle \approx 1.3$ to $(10.6 \pm 1.9) \times 10^9 M_\odot$ at $\langle z \rangle \approx 1.0$, i.e., by a factor $\gtrsim 3$. We thus find direct evidence that accretion of HI onto star-forming galaxies at $z \approx 1$ is insufficient to replenish their HI reservoirs and sustain their SFRs, thus resulting in the decline in the cosmic SFR density 8 billion years ago.

1. Introduction

Understanding the evolution of star formation activity in galaxies is a key open issue in galaxy evolution (e.g., Madau & Dickinson 2014). The cosmic comoving star formation rate (SFR) density of the universe is known to peak in the redshift range $z \approx 1–3$ and to then decline by an order of magnitude over the next ≈ 8 billion years to its value today (e.g., Le Floc'h et al. 2005; Bouwens et al. 2010). Approximately 90% of cosmic star formation at $z \lesssim 2.5$ takes place in galaxies lying on the galaxy "main sequence", a power-law relation between the SFR and the stellar mass followed by most star-forming galaxies at any redshift (e.g., Noeske et al. 2007; Rodighiero et al. 2011). The "amplitude" of the main sequence, i.e., the SFR at a fixed stellar mass, has been found to decline by a factor of ≈ 10 between $z \approx 1$ and $z \approx 0$ (e.g., Whitaker et al. 2014), similar to the decline in the cosmic SFR density over the same period. The cause of the decline in the star formation activity of the universe from $z \approx 1$ to $z \approx 0$ remains unknown today. Addressing this issue requires us to understand the evolution of the gas mass of galaxies, the fuel from which the stars form.

The primary fuel for star formation is neutral atomic hydrogen (HI). The atomic gas content of galaxies is best measured with the hyperfine HI 21 cm transition in the HI ground state, at a wavelength of ≈ 21.11 cm. Unfortunately, the low Einstein A coefficient of this transition has meant that even deep observations with the best radio telescopes today are only able to detect HI 21 cm emission from individual galaxies at low redshifts, $z \lesssim 0.4$ (e.g., Fernández et al. 2016). However, the average HI mass of a sample of galaxies can be measured by "stacking" the HI 21 cm emission signals from a large number of galaxies with known spatial positions and redshifts (e.g., Zwaan 2000; Chengalur et al. 2001; Lah et al. 2007; Kanekar et al. 2016; Bera et al. 2019). Such HI 21 cm-stacking studies have been used to estimate the average HI mass of star-forming galaxies out to $z \approx 1.3$ (Chowdhury et al. 2020, 2021).

Recently, Chowdhury et al. (2020) applied the HI 21 cm-stacking technique to galaxies in the DEEP2 fields to obtain the first detection of the average HI 21 cm emission signal from star-forming galaxies at $z \gtrsim 1$ (see also Chowdhury et al. 2021). Their results suggested that a decline in the HI reservoir of star-forming galaxies at $z \gtrsim 1$ could account for the observed decline in the SFR density of the universe at later times. In this Letter, we report first results from the Giant Metrewave Radio Telescope (GMRT) Cold-HI AT $z \approx 1$ (CATz1) Survey, a 510 hr upgraded GMRT HI 21 cm emission survey of the DEEP2 fields designed to directly probe the cause of the decline in the cosmic SFR density by measuring redshift evolution in the average HI mass of star-forming galaxies around $z \approx 1$ when the star formation activity of the universe begins to decline rapidly.[1]

2. Observations and Data Analysis

The GMRT-CATz1 survey is a deep HI 21 cm emission survey of galaxies at $z = 0.74–1.45$ with the upgraded GMRT (Swarup et al. 1991; Gupta et al. 2017) Band 4 receivers,

---

[1] Throughout this work, we use a flat "737" Lambda-cold dark matter cosmology, with $\Omega_m = 0.3$, $\Omega_\Lambda = 0.7$, and $H_0 = 70$ km s^{-1} Mpc^{-1}.

targeting three fields of the DEEP2 Galaxy Redshift Survey (Newman et al. 2013). The survey uses the H I 21 cm-stacking approach to carry out the first characterization of the H I properties of galaxies at $z \approx 1$. The DEEP2 Survey is uniquely suited to this experiment because it provides high-accuracy (≈ 55 km s^{-1}; Newman et al. 2013) measurements of the spectroscopic redshifts of galaxies at $z = 0.74$–1.45, whose H I 21 cm lines are redshifted into the GMRT Band 4 frequency coverage (≈ 550–830 MHz), and which are located in sky regions that are well matched to the GMRT Band 4 field of view (e.g., Kanekar et al. 2016; Chowdhury et al. 2020, 2021). The survey design, the observations, and the analysis of the GMRT-CATz1 survey data are described in detail in A. Chowdhury et al. (2022, in preparation). We provide here a brief summary of the observations and the analysis procedure.

The survey was carried out over three GMRT observing cycles, using 90 hr in 2018 October–2019 March (presented in Chowdhury et al. 2020), 170 hr in 2019 October–2020 March, and 250 hr in 2020 May–October (proposals 35_087, 37_063, and 38_033; PI: A. Chowdhury). The total time of ≈ 510 hr was divided approximately equally between the seven DEEP2 subfields (21, 22, 31, 32, 33, 41, and 42); the total on-source time on each subfield was ≈ 50–60 hr. We used the GMRT Wideband Backend as the correlator, with a total bandwidth of 400 MHz covering the frequency range 530–930 MHz and divided into 8192 spectral channels.

The data were analyzed in the Common Astronomy Software Applications package (CASA Version 5; McMullin et al. 2007) following standard procedures (e.g., Chowdhury et al. 2020) to produce the final continuum images and spectral cubes for each of the seven DEEP2 subfields. The AOFLAGGER package (Offringa et al. 2012) was used to excise data affected by radio frequency interference (RFI). For each DEEP2 subfield, we chose to carry out an independent analysis of the data from the different GMRT observing cycles. Treating the data of different cycles independently prevents systematic errors (due to, e.g., low-level RFI, imperfect deconvolution, etc.) in the data of one cycle from affecting the entire data set.

Our analysis yielded a total of 19 spectral cubes, 2 each for DEEP2 subfields 21 and 22 (which were each observed in only 2 GMRT cycles), and 3 each for DEEP2 subfields 31, 32, 33, 41, and 42 (which were each observed in all 3 GMRT cycles). The spectral cubes have a channel width of 48.8 kHz, corresponding to a velocity resolution of 18–25 km s^{-1} across our frequency coverage. The FWHMs of the synthesized beams of the cubes (i.e., the angular resolutions of the cubes) are $4''0$–$7''5$, corresponding to spatial resolutions of 29–63 kpc for the redshift range $z = 0.74$–1.45.

The analysis also yielded 655 MHz continuum images of the seven DEEP2 subfields, with root mean square (RMS) noise values of ≈ 5–10 μJy Beam^{-1} in the central regions of the images and synthesized-beam FWHMs of $\approx 3''$–$4''$ (A. Chowdhury et al. 2022, in preparation).

2.1. HI 21 cm Emission Stacking

The upgraded GMRT observations covered the redshifted H I 21 cm line for 16,250 galaxies at $z = 0.74$–1.45, for which the H I 21 cm lines are redshifted to 580–820 MHz, and that lie within the FWHM of the GMRT primary beam at the redshifted H I 21 cm line frequency of the galaxy. The FWHM of the GMRT primary beam was assumed to be $\approx 43'$ at

610 MHz; the primary-beam FWHM scales $\propto 1/\nu$ with the observing frequency, ν.

We restricted the H I 21 cm stacking to blue, star-forming galaxies and hence excluded red galaxies and galaxies hosting active galactic nuclei (AGNs) from the sample. We excluded 2222 red galaxies by only retaining objects with $C \leqslant 0$, where $C = U - B + 0.032 \times (M_B + 21.63) - 1.014$ (Willmer et al. 2006; Chowdhury et al. 2020). For AGNs, we excluded 882 DEEP2 objects that were detected at $\geqslant 4\sigma$ significance in our radio-continuum images, with 1.4 GHz luminosity $L_{1.4 \, \text{GHz}} \geqslant 2 \times 10^{23}$ W Hz^{-1} (Condon et al. 2002). We also excluded 487 galaxies with stellar mass $M_* < 10^9 M_\odot$, to ensure that our results can be directly compared with results for the xGASS survey at $z \approx 0$ (Catinella et al. 2018). Finally, we carried out a suite of statistical tests on the H I 21 cm spectra of individual galaxies to exclude any galaxies whose spectra are affected by non-Gaussian systematic effects (Chowdhury et al. 2020, A. Chowdhury et al. 2022, in preparation).

After the above exclusions, the main sample of the GMRT-CATz1 survey contains 11,419 blue star-forming galaxies with accurate redshifts (redshift quality, $Q \geqslant 3$, in the DEEP2 DR4 catalog; Newman et al. 2013) at $z = 0.74$–1.45, for which the H I 21 cm line is redshifted to ≈ 580–820 MHz (i.e., to frequencies where the Band 4 receivers have a high sensitivity), and that lie within the FWHM of the GMRT primary beam at the redshifted H I 21 cm frequency of the galaxy. The galaxies have stellar masses $M_* \approx 10^9$–$10^{11} M_\odot$.

For each galaxy, we made spectral subcubes, centered on the galaxy's position and redshift, and covering ± 500 kpc around the galaxy position and the velocity range ± 1500 km s^{-1} around the galaxy redshift. Each subcube was resampled onto a grid in the galaxy's rest frame; the resampled subcubes have spatial and velocity resolutions of 90 kpc and 30 km s^{-1}, respectively. We also convolved the subcubes to coarser spatial resolutions ($\leqslant 200$ kpc) and find no evidence that the H I 21 cm emission is spatially resolved at the resolution of 90 kpc (A. Chowdhury et al. 2022, in preparation).

Our observations yielded multiple H I 21 cm subcubes, with uncorrelated statistical noise, for nearly every galaxy of our sample. For each galaxy, there are two to three independent H I 21 cm subcubes from the different GMRT cycles. In addition, some galaxies lie in the overlap regions of our GMRT pointings (A. Chowdhury et al. 2022, in preparation), yielding additional independent H I 21 cm subcubes. Overall, we obtain a total of 28,993 independent H I 21 cm subcubes for the 11,419 blue star-forming galaxies of our sample.

For each of the 28,993 H I 21 cm subcubes, the flux-density values were first scaled to correct for the primary-beam response at the galaxy's location in the GMRT primary beam. This was done using an azimuthally symmetric polynomial fit to measurements of the average primary-beam response of the GMRT Band 4 receivers. Next, we converted each subcube from flux-density (S) units to luminosity-density (L) units at the redshift of the DEEP2 galaxy by using the relation $L = 4\pi S D_L^2/(1 + z)$, where D_L is the luminosity distance of the galaxy.

The stacking of the H I 21 cm emission signals was done by performing a weighted average of the spectral subcubes, using the same weight for each spatial and velocity pixel, for different galaxy subsamples, to obtain an average H I 21 cm spectral cube for each set of stacked galaxies. The weights assigned to each subcube were specific to the goal of the stacking and were used

to control either the redshift or the stellar-mass distributions of the galaxies in different subsamples. The weights did not take into account the RMS noise of the individual spectral cubes. The determination of the weights for the H I 21 cm subcubes for the specific cases of the stellar-mass subsamples and the redshift subsamples is discussed later.

Finally, we fitted a second-order polynomial to each spatial pixel of the stacked H I 21 cm cube and then subtracted this out to obtain a residual spectral cube. The second-order polynomial fit was performed after excluding the central ± 250 km s^{-1} velocity range. We note that the exclusion of the velocity channels in the central ± 250 km s^{-1} range from the fit results in a slight increase in the spectral RMS noise of these channels.

The RMS noise on the stacked H I 21 cm spectral cube was determined via Monte Carlo simulations. In these simulations, we circularly shifted the central velocity of each galaxy by a random offset in the range ± 1500 km s^{-1} and then stacked the velocity-shifted H I 21 cm subcubes. The above procedure was repeated to obtain 10^4 realizations of the stacked H I 21 cm subcube. The RMS noise on every spatial and velocity pixel of the final stacked H I 21 cm cube was then estimated from these 10^4 Monte Carlo realizations.

Finally, the average H I mass of a given subsample of DEEP2 galaxies was obtained from the velocity-integrated H I 21 cm line luminosity density ($\int L_{HI} dV$, in units of Jy Mpc^2 km s^{-1}), measured from the stacked H I 21 cm cube, via the expression $M_{HI} = [1.86 \times 10^4 \times \int L_{HI} dV] \, M_\odot$. The integral was carried out after smoothing the stacked cube to a velocity resolution of 90 km s^{-1} and was measured from a contiguous range of spectral channels with $\geqslant 1.5\sigma$ significance at this velocity resolution.

2.2. Stacking the Rest-frame 1.4 GHz Continuum Emission

The average SFRs of the different galaxy subsamples were measured by stacking their rest-frame 1.4 GHz radio luminosities (e.g., White et al. 2007; Bera et al. 2018; Chowdhury et al. 2020) using the correlation between the far-infrared and radio luminosities (e.g., Condon 1992; Yun et al. 2001). The radio-continuum stacking was performed by extracting a subimage of each galaxy from the full continuum image of its DEEP2 subfield and then smoothing and regridding each subimage to a spatial resolution of 40 kpc (at the galaxy redshift) and a uniform grid with 5.2 kpc pixels, extending ± 260 kpc around each galaxy. We note that the spatial resolution of 40 kpc is much larger than the typical size, ≈ 8 kpc, of the star-forming regions of galaxies at these redshifts (e.g., Trujillo et al. 2004). The flux-density values at the observed frequency in every pixel of each subimage were scaled to the corresponding rest-frame 1.4 GHz flux densities at the galaxy's redshift, assuming a spectral index of $\alpha = -0.8$ (Condon 1992), with flux density $S_\nu \propto \nu^\alpha$. Next, we converted the rest-frame flux density ($S_{1.4 \, GHz}$) of every pixel of each subimage to luminosity-density ($L_{1.4 \, GHz}$) units using the relation $L_{1.4 \, GHz} = 4\pi \, S_{1.4 \, GHz} \, D_L^2 / (1 + z)$, where D_L is the luminosity distance of the galaxy. The stacked rest-frame 1.4 GHz luminosity was computed by taking a weighted median of the rest-frame 1.4 GHz luminosities of the corresponding spatial pixels of the different subimages, across the subsample of galaxies; the weights were chosen such that each galaxy has the same effective weight as in the H I 21 cm stack of the same subsample. The median rest-frame 1.4 GHz luminosity was then converted to a median SFR using the relation SFR $(M_\odot / \text{yr}) = (3.7 \pm 1.1) \times 10^{-22} \times L_{1.4 \, GHz}(W/Hz)$ (Yun et al. 2001; scaled to a Chabrier

IMF). Finally, for each stacked image, we corrected the rest-frame 1.4 GHz luminosity for a small zero-point offset ($\approx 0.4 \, \mu$Jy/Beam), at the level of 2%–10% of the measured value; the offset was estimated by applying the above stacking procedure to subimages at locations offset by 100″ from the DEEP2 galaxies of the sample.

We note that our radio-derived SFR estimates are affected by uncertainties in the flux-density scale of our radio-continuum images. These systematic uncertainties are typically $\lesssim 10\%$ for the GMRT for our calibration procedure. Thus, all quoted errors on our SFR values have been estimated by adding, in quadrature, a 10% systematic uncertainty to the 1σ statistical uncertainty.

3. Results and Discussion

Galaxies lying on the star-forming main sequence dominate the SFR density of the universe out to $z \approx 2.5$ (Rodighiero et al. 2011). The decline in the SFR density of the universe at $z \lesssim 1$ is caused by a decline in the zero-point of the star-forming main sequence (e.g., Whitaker et al. 2014; Leslie et al. 2020). We compared the stellar masses and SFRs of our sample of 11,419 galaxies with measurements of the star-forming main-sequence at these redshifts to determine if the sample galaxies are representative of main-sequence galaxies. This was done by dividing the sample of 11,419 galaxies into two redshift intervals, $z = 0.74$–1.00 and $z = 1.00$–1.45, and further dividing the galaxies in each redshift interval into multiple stellar-mass subsamples, each of width 0.5 dex. We then used the procedure of Section 2.2 to stack the rest-frame 1.4 GHz continuum emission of the galaxies in each subsample to determine their average SFRs. For the two redshift intervals, we used weights during the stacking process to ensure that the redshift distributions of the stellar-mass subsamples are identical. The average stellar mass and the average SFR of each subsample, for both redshift intervals, are shown in Figure 1(A). The figure also shows, for comparison, the star-forming main sequence in the same redshift intervals, from Whitaker et al. (2014). Figure 1(A) shows that the average SFR and the average stellar mass of the galaxies in each subsample are consistent with the star-forming main sequence in both redshift intervals (see also A. Chowdhury et al. 2022., in preparation). Our sample of 11,419 blue star-forming galaxies at $z = 0.74$–1.45 is thus representative of main-sequence galaxies at these redshifts.

Detailed characterizations of the main sequence (Whitaker et al. 2014; Leslie et al. 2020) and the stellar-mass function of high-z galaxies (Davidzon et al. 2017) have shown that the decline in the cosmic SFR density at $z \lesssim 1$ is predominantly due to the decline in the SFR density of the most massive galaxies, with stellar masses $M_* \gtrsim 10^{10} \, M_\odot$. We combined the star-forming main sequence (Whitaker et al. 2014) and the stellar-mass function of galaxies (Davidzon et al. 2017) to estimate the cosmic SFR density of galaxies as a function of their stellar mass. Figure 1(B) shows the cosmic SFR density of galaxies as a function of their stellar mass in two redshift intervals, with mean redshifts of $\langle z \rangle = 1.3$ and $\langle z \rangle = 0.95$, respectively. Star-forming galaxies with $M_* \gtrsim 10^{10} \, M_\odot$, shown as the shaded region in Figure 1(B), contribute $\approx 85\%$ to the decline in the total SFR density from $z \approx 1.3$ to $z \approx 0.95$. Maintaining the H I reservoir in such galaxies would require accretion to take place at a high rate. If the lack of gas accretion in galaxies causes the decline of the cosmic SFR density at
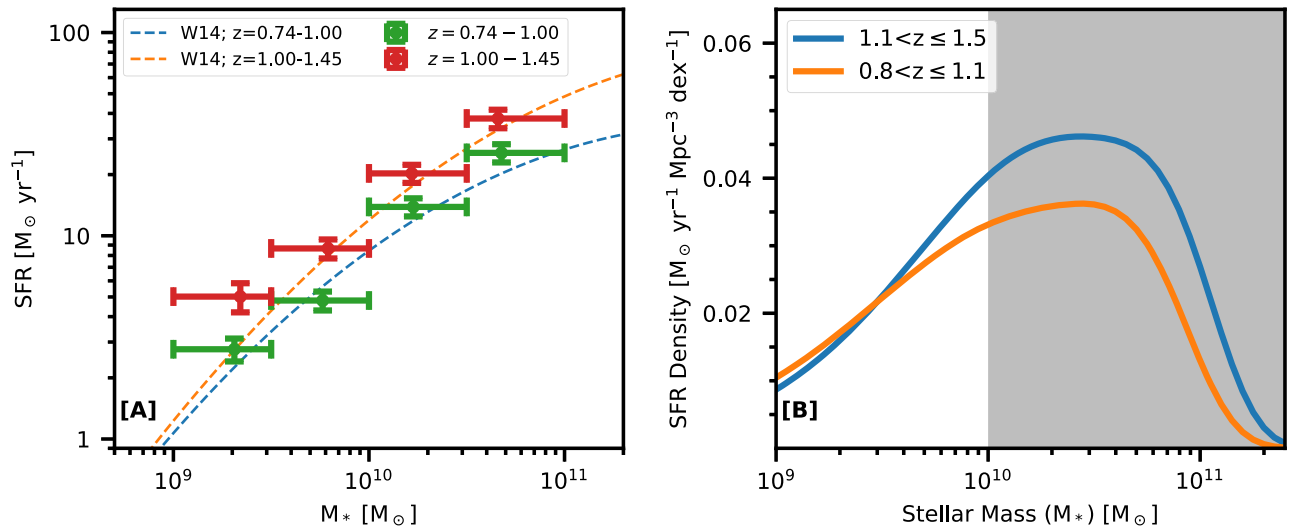
Figure 1. (A) The average SFR and the average stellar mass of our sample of 11,419 galaxies. The green and red points show, respectively, the average SFRs of the subsamples of galaxies at $z = 0.74$–1.00 and $z = 1.00$–1.45, in stellar-mass bins of width 0.5 dex. The dotted lines show the star-forming main sequence of Whitaker et al. (2014), interpolated to the same redshift intervals. The average stellar mass and the average SFR of galaxies in each subsample are seen to be consistent with the star-forming main sequence. (B) The contribution of star-forming galaxies to the cosmic SFR density (see also Leslie et al. 2020). The figure shows the cosmic SFR density as a function of the stellar mass of galaxies in two redshift bins: (i) during the epoch of peak cosmic SFR density, $z = 1.1$–1.5 (blue), and (ii) after the epoch of peak cosmic SFR density, $z = 0.8$–1.1 (orange). Star-forming galaxies with $M_* \geqslant 10^{10}\,M_\odot$ (shown in the shaded region) dominate the SFR density at both epochs and contribute $\approx 85\%$ to the decline in the cosmic SFR density at $z \lesssim 1$.
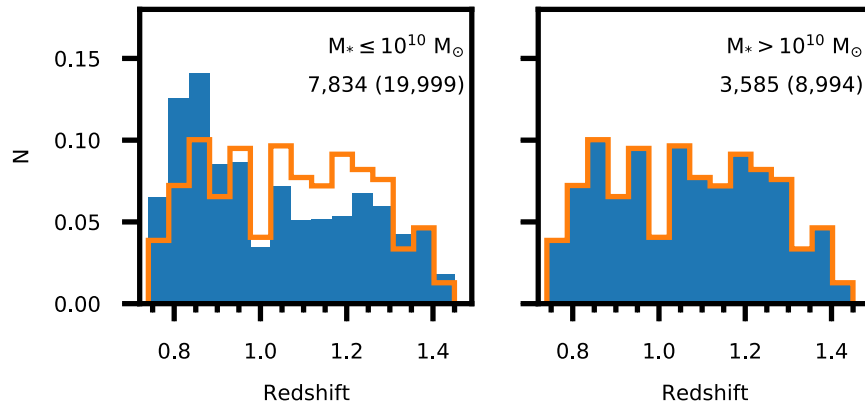

Figure 2. The redshift distributions of galaxies in the two stellar-mass subsamples. The blue histograms show the number of H I 21 cm subcubes as a function of redshift in each of the two stellar-mass subsamples; each histogram has been normalized by the total number of subcubes in its subsample. The orange histogram in each panel shows the redshift distribution of galaxies in the high stellar-mass subsample. The H I 21 cm subcubes of the lower stellar-mass subsample were assigned weights such that their effective redshift distribution is the one shown in orange, i.e., is identical to that of the higher stellar-mass subsample. The number of galaxies in each subsample is shown above each histogram, with the number of H I 21 cm subcubes in parentheses.

$z \lesssim 1$, one would expect that the most massive galaxies, which dominate the SFR density at these redshifts, would consume the bulk of their H I reservoir on a very short timescale, comparable to the ≈ 1 billion year interval between $z \approx 1.3$ and $z \approx 1.0$.

3.1. Very Short H I Depletion Timescale in Massive Galaxies

We hence examined the dependence of the average H I mass and the H I depletion timescale on the average stellar mass by dividing the full sample of 11,419 galaxies into two subsamples, with (A) $M_* \lesssim 10^{10}\,M_\odot$ (7834 galaxies and 19,999 independent H I 21 cm subcubes) and (B) $M_* > 10^{10}\,M_\odot$ (3585 galaxies and 8994 independent subcubes). Figure 2 shows the redshift distributions of the H I 21 cm subcubes in each of the two stellar-mass subsamples. It is clear that the lower stellar-mass subsample contains more galaxies at lower redshifts than the higher stellar-mass subsample; this is

because the DEEP2 survey is a magnitude-limited survey and is hence biased toward detecting fainter (i.e., typically less massive) galaxies at lower redshifts. We account for this difference in the redshift distributions of the two stellar-mass subsamples by assigning weights to each galaxy to ensure that the effective redshift distribution of the two stellar-mass subsamples is identical. Specifically, we assigned weights to the H I 21 cm subcubes in the low stellar-mass subsample to make their effective redshift distribution identical to that of the H I 21 cm subcubes in the high stellar-mass subsample. These weights were then used in stacking both the H I 21 cm emission and the rest-frame 1.4 GHz radio continuum of the galaxies of each subsample, following the procedures in Sections 2.1 and 2.2, to determine the average H I mass and the average SFR of galaxies in the two subsamples. These weights were further used in the determination of all average quantities for the two stellar-mass subsamples. In passing, we note that the effective
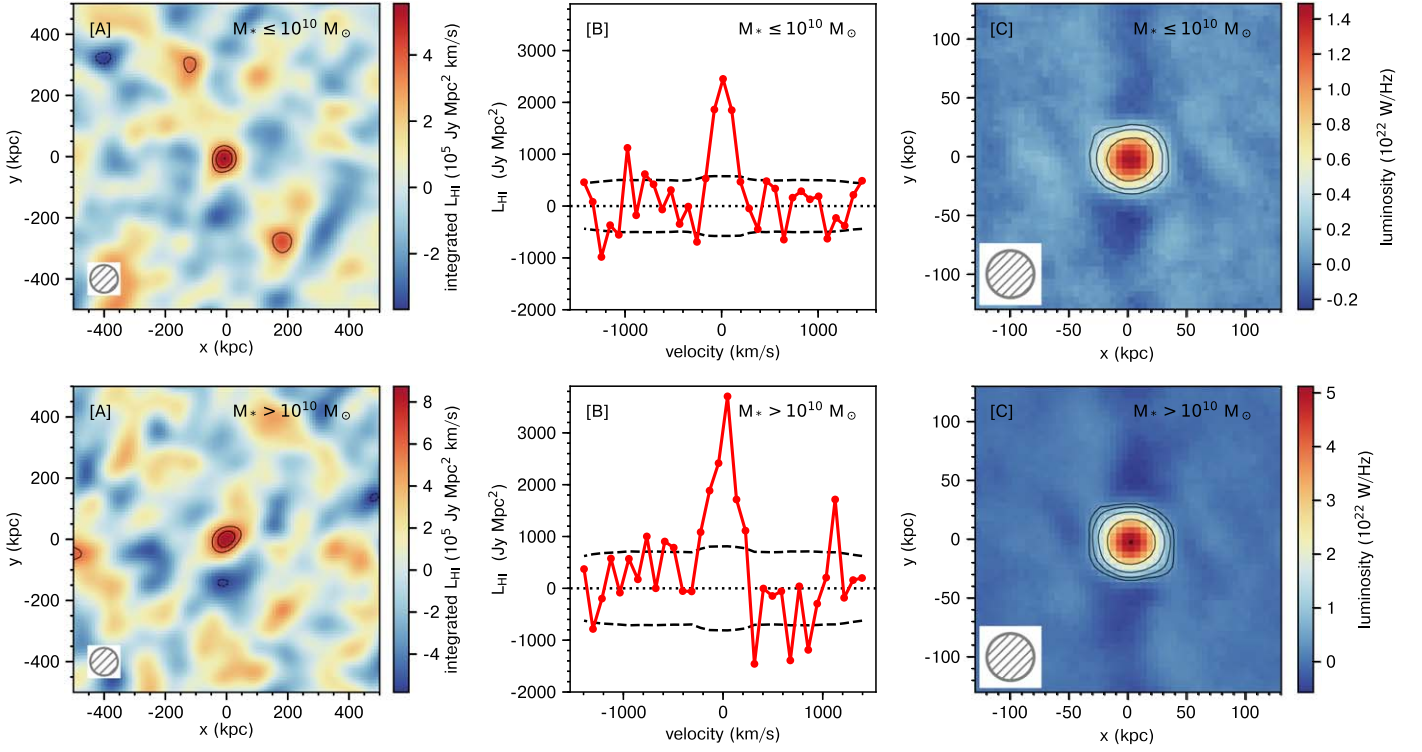
Figure 3. The stacked H I 21 cm emission and the stacked rest-frame 1.4 GHz continuum emission from star-forming galaxies with different stellar masses at $z \approx 1$. (A) The left panels show, for the two stellar-mass subsamples, the average H I 21 cm emission images. The circle on the bottom left of each panel shows the 90 kpc spatial resolution of the images. The contour levels are at -3.0σ (dashed), $+3.0\sigma$, $+4.0\sigma$, and $+5.0\sigma$ significance. (B) The middle panels show the average H I 21 cm emission spectra for the two subsamples; the channel width is 90 km s^{-1}, and the dashed curves show the $\pm1\sigma$ error on each spectrum. The average H I 21 cm emission signals from both subsamples are clearly detected in both the images and the spectra. (C) The right panels show the stacked rest-frame 1.4 GHz luminosity images of the galaxies in the two subsamples. The contour levels are at 5σ, 10σ, 20σ, 40σ, and 80σ statistical significance. The circle at the bottom left of each panel shows the 40 kpc resolution of the images. The average rest-frame 1.4 GHz continuum emission is detected at high ($>37\sigma$) significance in both images.

redshift distribution of the two subsamples has a mean of $\langle z \rangle \approx 1.1$.

Figure 3 shows the stacked H I 21 cm emission image, the stacked H I 21 cm spectrum, and the stacked rest-frame 1.4 GHz continuum image of the galaxies in each of the two stellar-mass subsamples. We obtain clear detections of the average H I 21 cm emission signal from both subsamples, each at $>4.6\sigma$ statistical significance, as well as detections of the rest-frame 1.4 GHz luminosity, each at $>37\sigma$ significance. This allows us to determine the average H I mass and the average SFR of the galaxies of each stellar-mass subsample.

The H I depletion timescale, $t_{\rm dep,HI} = M_{\rm HI}/{\rm SFR}$, quantifies the timescale on which a galaxy would convert its entire H I reservoir into stars if it continues to form stars at its current SFR. Star formation would be quenched in a galaxy on timescales longer than $\approx t_{\rm dep,HI}$, if the H I reservoir is not replenished by the accretion of gas from the circumgalactic medium or by minor mergers. We combined our estimates of the average H I mass and the average SFR in the two stellar-mass subsamples to estimate $\langle t_{\rm dep,HI} \rangle \equiv \langle M_{\rm HI} \rangle / \langle {\rm SFR} \rangle$ for each subsample. The inferred average stellar mass, average H I mass, average SFR, and average H I depletion timescale of the two stellar-mass subsamples are listed in the last four rows of Table 1.

Figure 4 plots the average H I depletion timescale of the two stellar-mass subsamples against their average stellar mass. For comparison, we also plot $\langle t_{\rm dep,HI} \rangle$ against average stellar mass for a reference sample of $z \approx 0$ galaxies, the stellar-mass-selected xGASS sample (Catinella et al. 2018). For the xGASS galaxies, we have restricted these to blue galaxies, with

NUV $- r < 4$, and used weights to obtain an effective stellar-mass distribution matched to that of the DEEP2 subsamples. We find that the average H I depletion timescale of DEEP2 galaxies with $M_* \lesssim 10^{10} M_\odot$ is ≈ 2 Gyr, a factor of ≈ 3 smaller than that of similar galaxies in the local universe. However, remarkably, we find a far shorter average H I depletion timescale, $\langle t_{\rm dep,HI} \rangle = 0.86 \pm 0.20$ Gyr, in the most massive DEEP2 galaxies, with $M_* > 10^{10} M_\odot$, at $z \approx 1.1$. This is comparable to the ≈ 1.0 Gyr period between $z = 1.3$ and $z = 1$ (corresponding to lookback times of ≈ 9 Gyr and 8 Gyr, respectively) and to the molecular gas depletion timescale, $t_{\rm dep,H_2} \approx 0.7$ Gyr, for similar galaxies at these redshifts (Tacconi et al. 2013). Star-forming galaxies with $M_* > 10^{10} M_\odot$ would thus be able to sustain their SFR for only about a billion years unless their H I is replenished on this timescale via accretion from the circumgalactic medium or mergers. The very short H I depletion timescale in the most massive galaxies, which dominate the decline in the cosmic SFR density at $z \lesssim 1$, is consistent with the hypothesis that most of the H I in such galaxies was consumed by $z \approx 1$ and that the lack of accretion of H I onto such galaxies led to the quenching of their star formation and hence to the decline in the cosmic SFR density at $z \lesssim 1$.

3.2. Rapid Redshift Evolution in the H I Mass of Star-forming Galaxies over z ≈ 0.74–1.45

The redshift coverage of the GMRT CATz1 survey covers both the peak of the cosmic SFR density at $z \gtrsim 1$ and the decline of the SFR density at $z \lesssim 1$. This allows us to directly

Table 1
Average Properties of Galaxies in the Stellar Mass and the Redshift Subsamples

	Stellar-mass Subsamples		Redshift Subsamples	
	Low	High	Low	High
Stellar-mass range ($\times 10^9 \, M_\odot$)	1.0–10	10–240	1.0–240	1.0–240
Redshift range	0.74–1.45	0.74–1.45	0.74–1.25	1.25–1.45
Number of galaxies	7834	3585	9284	2135
Number of HI 21 cm subcubes	19,999	8994	23,630	5363
Average redshift, $\langle z \rangle$	1.1	1.1	0.98	1.33
Average stellar mass ($\times 10^9 \, M_\odot$)	4.9	21.4	10.3	10.3
Average HI mass ($\times 10^9 \, M_\odot$)	10.4 ± 2.1	16.3 ± 3.5	10.6 ± 1.9	33.6 ± 6.4
Average SFR ($M_\odot \, \mathrm{yr}^{-1}$)	5.5 ± 0.6	18.9 ± 1.9	7.5 ± 0.8	15.8 ± 1.7
Average HI depletion timescale (Gyr)	1.93 ± 0.44	0.86 ± 0.20	1.41 ± 0.31	2.01 ± 0.37

Note. For each of the two stellar-mass subsamples (columns 2 and 3) and the two redshift subsamples (columns 4 and 5), the rows are (1) the range of stellar masses, (2) the number of galaxies in each subsample, (3) the number of HI 21 cm subcubes in each subsample, (4) the average redshift of the galaxies in each subsample, after applying the weights, (5) the average stellar mass of the galaxies in each subsample, after applying the weights, (6) the average HI mass of the galaxies in each subsample, (7) the average SFR of the galaxies in each subsample, and (8) the average HI depletion timescale, $\langle t_{\mathrm{dep,HI}} \rangle \equiv \langle M_{\mathrm{HI}} \rangle / \langle \mathrm{SFR} \rangle$, of the galaxies in each subsample. See the main text for a description of the weights that were applied to different subsamples. We note that the distribution of the galaxies within the GMRT primary beam, as a function of the distance from the pointing center, is very similar for all four subsamples.

test the hypothesis that insufficient gas accretion caused the decline in the cosmic SFR density by measuring the HI content of star-forming galaxies of the same stellar mass in two redshift bins, with average redshifts $\langle z \rangle \approx 1.3$ and $\langle z \rangle \approx 1$. If the HI reservoir of star-forming galaxies at $z \approx 1.3$ is indeed not replenished by accretion, we expect to observe a significant decline in the average HI mass of such galaxies, from $\langle z \rangle = 1.3$ to $\langle z \rangle = 1$.

To test this hypothesis, we divided our sample of 11,419 star-forming galaxies into two subsamples based on the galaxy redshift. The high-redshift sample includes 2135 galaxies (5363 independent HI 21 cm subcubes) at $z = 1.25$–1.45 (i.e., during the epoch of the peak of cosmic SFR density, with an average redshift $\langle z \rangle \approx 1.3$), while the low-redshift sample contains 9284 galaxies (23,630 independent subcubes) at $z = 0.74$–1.25 (i.e., covers the decline of the cosmic SFR density, with $\langle z \rangle \approx 1.0$). The intrinsic stellar-mass distributions of the two subsamples, shown in Figure 5, are different. We corrected for this effect by assigning weights to each galaxy in the lower-redshift subsample to ensure that the stellar-mass distributions of the two subsamples are identical; the weighted-mean stellar mass of each subsample is $\approx 10^{10} \, M_\odot$.

Using the above weights, we stacked the HI 21 cm subcubes and the rest-frame 1.4 GHz continuum subimages of the galaxies in the two redshift subsamples, following the procedures of Sections 2.1 and 2.2. This yielded clear detections of the average HI 21 cm emission signal (with $>5.2\sigma$ statistical significance) and the average rest-frame 1.4 GHz luminosity (with $>32\sigma$ statistical significance) from both subsamples. Figure 6 shows the stacked HI 21 cm emission image, the stacked HI 21 cm spectrum, and the stacked rest-frame 1.4 GHz radio-continuum image of the galaxies in the two redshift subsamples. We find that star-forming galaxies with $\langle M_* \rangle \approx 10^{10} \, M_\odot$ at $\langle z \rangle \approx 1.0$ have an average HI mass of $M_{\mathrm{HI}} = (10.6 \pm 1.9) \times 10^9 \, M_\odot$, while those at $\langle z \rangle \approx 1.3$ have an average HI mass of $M_{\mathrm{HI}} = (33.6 \pm 6.4) \times 10^9 \, M_\odot$. We thus find evidence, at 3.4σ statistical significance, that the average HI mass of star-forming galaxies with $\langle M_* \rangle \approx 10^{10} \, M_\odot$ at $\langle z \rangle \approx 1.3$ is higher, by a factor of ≈ 3.2, than that of galaxies with an identical stellar-mass distribution at $\langle z \rangle \approx 1.0$. Finally, stacking the 1.4 GHz luminosities of the two subsamples yields average SFRs of $(15.8 \pm 1.6) \, M_\odot \, \mathrm{yr}^{-1}$ at $\langle z \rangle \approx 1.3$ but only
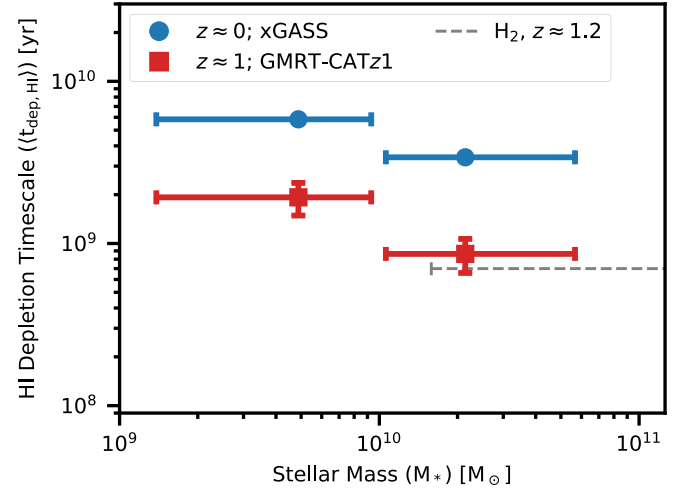

Figure 4. The average HI depletion timescale, $\langle t_{\mathrm{dep,HI}} \rangle \equiv \langle M_{\mathrm{HI}} \rangle / \langle \mathrm{SFR} \rangle$, of star-forming galaxies at $z \approx 1.1$, plotted against the average stellar mass. The red circles show our measurements of the average HI depletion timescale for the two stellar-mass subsamples. The error bars along the y-axis indicate the 1σ statistical uncertainties on the measurements while the error bars along the x-axis show the 90% range of stellar masses in each subsample. The blue points show the average HI depletion timescale, $\langle t_{\mathrm{dep,HI}} \rangle \equiv \langle M_{\mathrm{HI}} \rangle / \langle \mathrm{SFR} \rangle$, for two subsamples of xGASS galaxies at $z \approx 0$ (Catinella et al. 2018), each with the same stellar-mass distribution as the corresponding DEEP2 subsample. The dashed gray line shows the H_2 depletion timescale of star-forming galaxies at $z \approx 1.2$ (Tacconi et al. 2013). We obtain a very short average HI depletion timescale, ≈ 0.86 Gyr, for star-forming galaxies with $M_* > 10^{10} \, M_\odot$ at $z \approx 1.1$, comparable to the H_2 depletion timescale (Tacconi et al. 2013) in similar galaxies at $z \approx 1.2$.

$(7.5 \pm 0.8) \, M_\odot \, \mathrm{yr}^{-1}$ at $\langle z \rangle \approx 1.0$. We thus find direct evidence that the HI reservoir of star-forming galaxies is indeed rapidly depleted between $z \approx 1.3$ and $z \approx 1.0$, i.e., on a timescale of ≈ 1 billion years. The decline in HI mass is by a factor of (3.2 ± 0.8), consistent with the decline in the average SFR, by a factor of (2.1 ± 0.3), of the same galaxies over the same redshift interval.

Figure 7 plots the average HI mass of the DEEP2 galaxies in the two redshift subsamples against redshift, along with the average HI mass of blue xGASS galaxies at $z \approx 0$, again with weights chosen to yield the same stellar-mass distribution as
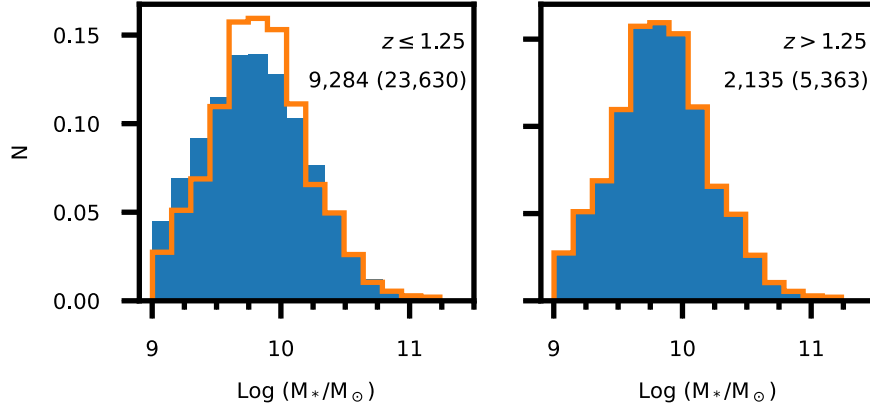
Figure 5. The stellar-mass distributions of galaxies in the two redshift subsamples. The blue histogram shows the number of H I 21 cm subcubes, in bins of stellar mass, in the two redshift subsamples; each histogram has been normalized by the total number of subcubes in its subsample. The orange histograms show the stellar-mass distribution of galaxies at $z = 1.25$–1.45. The galaxies in the lower-redshift subsample were assigned weights such that their effective stellar-mass distribution is the one shown in orange, i.e., is identical to the stellar-mass distribution of galaxies in the higher-redshift subsample. The number of galaxies in each subsample is shown above the histogram, with the number of H I 21 cm subcubes shown in parentheses.
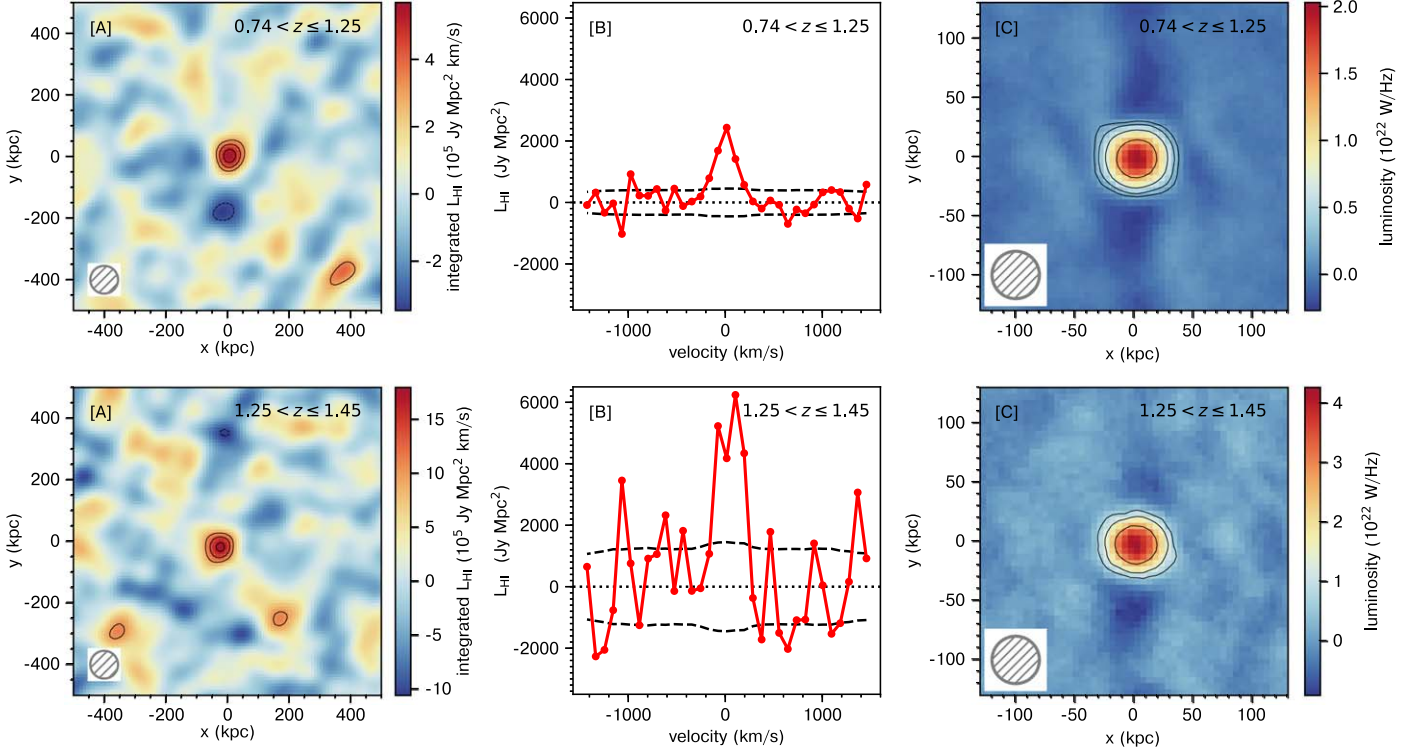

Figure 6. The average H I 21 cm emission and the average rest-frame 1.4 GHz continuum emission from star-forming galaxies in the two redshift subsamples. (A) The left panels show, for the two stellar-mass subsamples, the stacked H I 21 cm emission images. The circle at the bottom left of each panel shows the 90 kpc spatial resolution of the images. The contour levels are at -3.0σ (dashed), $+3.0\sigma$, $+4.0\sigma$, and $+5.0\sigma$ significance. (B) The middle panels show the average H I 21 cm emission spectra; the channel width is 90 km s^{-1}, while the dashed curves show the $\pm 1\sigma$ error on each spectrum. The stacked H I 21 cm emission signals from both subsamples are clearly detected in both the images and the spectra. (C) The right panels show the stacked rest-frame 1.4 GHz luminosity images of the galaxies in the two subsamples. The contour levels are at 5σ, 10σ, 20σ, and 40σ statistical significance. The circle at the bottom left of each panel shows the 40 kpc resolution of the images. The average rest-frame 1.4 GHz continuum emission is clearly detected at high ($>32\sigma$) significance in both images.

that of the high-z galaxies. The average H I mass[2] of blue xGASS galaxies with $\langle M_* \rangle \approx 10^{10} M_\odot$ is $(4.1 \pm 0.2) \times 10^9 M_\odot$. This is a factor of ≈ 2.6 lower than the average H I mass of our lower-redshift subsample, $M_{\mathrm{HI}} = (10.6 \pm 1.9) \times 10^9 M_\odot$ at $\langle z \rangle \approx 1.0$. We thus also find evidence (at $\approx 3.4\sigma$ significance) for evolution in the average H I mass of star-forming galaxies with the same stellar-mass distribution

between $z \approx 1$ and $z \approx 0$. Overall, Figure 7 shows that the average H I mass in galaxies with $\langle M_* \rangle \approx 10^{10} M_\odot$ rapidly declines, by a factor of ≈ 3.2, over a period of ≈ 1 billion years from $z \approx 1.3$ and $z \approx 1.0$, and then gradually declines, by a factor of ≈ 2.6, over the next ≈ 8 billion years from $z \approx 1$ to $z \approx 0$.

Finally, we investigated the possibility that our measurement of the decline in the average H I mass of star-forming galaxies from $z \approx 1.3$ to $z \approx 1.0$ might be caused by incompleteness issues in the DEEP2 sample. First, we note that the galaxies in both
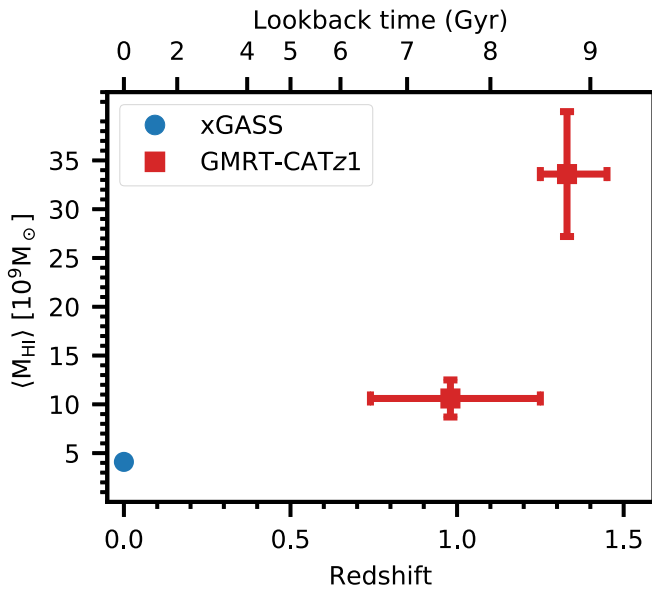
---

[2] The error on the average H I mass of the xGASS galaxies was computed using bootstrap resampling with replacement.

Figure 7. The redshift evolution of the average H I mass of star-forming galaxies over $z = 0.74$–1.45. The red squares show our measurements of the average H I mass of star-forming galaxies in the two redshift subsamples at $\langle z \rangle \approx 1.3$ and $\langle z \rangle \approx 1.0$, with identical stellar-mass distributions, obtained by separately stacking the H I 21 cm signals of galaxies in each subsample. The average H I mass of blue xGASS galaxies at $z \approx 0$ (Catinella et al. 2018), with an identical effective stellar-mass distribution, is marked with a blue circle. The average H I mass is seen to decline steeply from $z \approx 1.3$ to $z \approx 1.0$, and then to decline slowly down to $z \approx 0$, for galaxies of the same average stellar mass, $\langle M_* \rangle \approx 10^{10} M_\odot$.

redshift subsamples are representative of the main-sequence population at their redshifts (see Figure 1(A)). We tested for incompleteness issues by restricting our analysis of the redshift evolution of the H I mass to only the most massive galaxies of the sample, with stellar masses greater than the median stellar mass, $6.3 \times 10^9 M_\odot$; such galaxies are much less likely to be affected by incompleteness. We divided this massive-galaxy sample of 5751 galaxies with $M_* > 6.3 \times 10^9 M_\odot$ into two redshift subsamples at $z = 0.74$–1.25 (4589 galaxies) and $z = 1.25$–1.25 (1162 galaxies) and separately stacked the H I 21 cm subcubes of the galaxies in each redshift subsample, following the procedures of Section 2.1, again ensuring that the stellar-mass distributions of the two subsamples are identical. We find that the average H I masses of star-forming galaxies with $\langle M_* \rangle \approx 1.6 \times 10^{10} M_\odot$ at $\langle z \rangle \approx 1.0$ and $\langle z \rangle \approx 1.3$ are $M_{\rm HI} = (16.0 \pm 3.2) \times 10^9 M_\odot$ and $M_{\rm HI} = (48 \pm 10) \times 10^9 M_\odot$, respectively. Thus, even for the massive-galaxy subsample, we continue to find evidence, at $\approx 3.0\sigma$ significance, for a decline in the average H I mass between $z \approx 1.3$ and $z \approx 1.0$. Overall, we do not find any evidence that the measurement of the redshift evolution of the average H I mass of main-sequence galaxies presented in this Letter might be affected by selection biases.

4. Summary

We report the first results from the GMRT-CATz1 survey, a 510 hr H I 21 cm emission survey of galaxies at $z = 0.74$–1.45 in the DEEP2 fields. We use stacking of the H I 21 cm emission and the rest-frame 1.4 GHz radio-continuum of subsamples of DEEP2 galaxies to determine the dependence of the average H I mass and the average H I depletion time of main-sequence galaxies at $z = 0.74$–1.45 on their average stellar mass and redshift. We find that H I plays a fundamental role in the decline

of the cosmic SFR density at $z \lesssim 1$. The very short average H I depletion timescale of ≈ 0.86 billion years in the most massive galaxies, which dominate the cosmic SFR density at $z > 1$, implies that rapid gas accretion is needed to maintain their H I reservoirs and sustain their high SFRs. And the sharp decline in the average H I mass of galaxies with $\langle M_* \rangle \approx 10^{10} M_\odot$, by a factor of ≈ 3.2 from $z \approx 1.3$ to $z \approx 1$, indicates that such efficient gas accretion does not take place. We conclude that the lack of accretion of H I onto the most massive star-forming galaxies toward the end of the epoch of peak cosmic SFR density causes the decline in the cosmic SFR density at $z \lesssim 1$, 8 billion years ago.

ORCID iDs

Aditya Chowdhury ⬤ https://orcid.org/0000-0002-5795-517X
Nissim Kanekar ⬤ https://orcid.org/0000-0002-9757-7206
Jayaram N. Chengalur ⬤ https://orcid.org/0000-0002-0269-1154

References

Astropy Collaboration, Price-Whelan, A. M., Sipőcz, B. M., et al. 2018, AJ, 156, 123
Astropy Collaboration, Robitaille, T. P., Tollerud, E. J., et al. 2013, A&A, 558, A33
Bera, A., Kanekar, N., Chengalur, J. N., & Bagla, J. S. 2019, ApJL, 882, L7
Bera, A., Kanekar, N., Weiner, B. J., Sethi, S., & Dwarakanath, K. S. 2018, ApJ, 865, 39
Bouwens, R. J., Illingworth, G. D., Oesch, P. A., et al. 2010, ApJL, 709, L133
Catinella, B., Saintonge, A., Janowiecki, S., et al. 2018, MNRAS, 476, 875
Chengalur, J. N., Braun, R., & Wieringa, M. 2001, A&A, 372, 768
Chowdhury, A. 2021, calR: Robust Calibration in CASA, v3.3.1, https://github.com/chowdhuryaditya/calR
Chowdhury, A., Kanekar, N., Chengalur, J. N., Sethi, S., & Dwarakanath, K. S. 2020, Natur, 586, 369
Chowdhury, A., Kanekar, N., Das, B., Sethi, S., & Dwarakanath, K. S. 2021, ApJL, 913, L24
Condon, J. J. 1992, ARA&A, 30, 575
Condon, J. J., Cotton, W. D., & Broderick, J. J. 2002, AJ, 124, 675
Davidzon, I., Ilbert, O., Laigle, C., et al. 2017, A&A, 605, A70
Fernández, X., Gim, H. B., van Gorkom, J. H., et al. 2016, ApJL, 824, L1
Gupta, Y., Ajithkumar, B., Kale, H. S., et al. 2017, CSci, 113, 707
Kanekar, N., Sethi, S., & Dwarakanath, K. S. 2016, ApJL, 818, L28
Lah, P., Chengalur, J. N., Briggs, F. H., et al. 2007, MNRAS, 376, 1357
Le Floc'h, E., Papovich, C., Dole, H., et al. 2005, ApJ, 632, 169
Leslie, S. K., Schinnerer, E., Liu, D., et al. 2020, ApJ, 899, 58
Madau, P., & Dickinson, M. 2014, ARA&A, 52, 415
McMullin, J. P., Waters, B., Schiebel, D., Young, W., & Golap, K. 2007, in ASP Conf. Ser. 376, CASA Architecture and Applications, ed. R. A. Shaw, F. Hill, & D. J. Bell (San Francisco, CA: ASP), 127
Newman, J. A., Cooper, M. C., Davis, M., et al. 2013, ApJS, 208, 5
Noeske, K. G., Weiner, B. J., Faber, S. M., et al. 2007, ApJL, 660, L43
Offringa, A. R., van de Gronde, J. J., & Roerdink, J. B. T. M. 2012, A&A, 539, A95

Rodighiero, G., Daddi, E., Baronchelli, I., et al. 2011, ApJL, 739, L40
Swarup, G., Ananthakrishnan, S., Kapahi, V. K., et al. 1991, CSci, 60, 95
Tacconi, L. J., Neri, R., Genzel, R., et al. 2013, ApJ, 768, 74
Trujillo, I., Rudnick, G., Rix, H.-W., et al. 2004, ApJ, 604, 521
Whitaker, K. E., Franx, M., Leja, J., et al. 2014, ApJ, 795, 104

White, R. L., Helfand, D. J., Becker, R. H., Glikman, E., & de Vries, W. 2007, ApJ, 654, 99
Willmer, C. N. A., Faber, S. M., Koo, D. C., et al. 2006, ApJ, 647, 853
Yun, M. S., Reddy, N. A., & Condon, J. J. 2001, ApJ, 554, 803
Zwaan, M. A. 2000, PhD Thesis, Groningen: Rijksuniversiteit